Nominally hydrous magmatism on the Moon

Francis M. McCubbin[a,1], Andrew Steele[a], Erik H. Hauri[b], Hanna Nekvasil[c], Shigeru Yamashita[d], and Russell J. Hemley[a]

[a]Geophysical Laboratory, Carnegie Institution of Washington, 5251 Broad Branch Road, N.W., Washington, DC 20015; [b]Department of Terrestrial Magnetism, Carnegie Institution of Washington, 5241 Broad Branch Road, N.W., Washington, DC 20015; [c]Department of Geosciences, Stony Brook University, Stony Brook, NY 11794; and [d]Institute for Study of the Earth's Interior, Okayama University, Misasa, Tottori 682-0193, Japan

For the past 40 years, the Moon has been described as nearly de-void of indigenous water; however, evidence for water both on the lunar surface and within the lunar interior have recently emerged, calling into question this long-standing lunar dogma. In the present study, hydroxyl (as well as fluoride and chloride) was analyzed by secondary ion mass spectrometry in apatite [$Ca_5(PO_4)_3(F,Cl,OH)$] from three different lunar samples in order to obtain quantitative constraints on the abundance of water in the lunar interior. This work confirms that hundreds to thousands of ppm water (of the structural form hydroxyl) is present in apatite from the Moon. Moreover, two of the studied samples likely had water preserved from magmatic processes, which would qualify the water as being indigenous to the Moon. The presence of hydroxyl in apatite from a number of different types of lunar rocks indicates that water may be ubiquitous within the lunar interior, potentially as early as the time of lunar formation. The water contents analyzed for the lunar apatite indicate minimum water contents of their lunar source region to range from 64 ppb to 5 ppm H_2O. This lower limit range of water contents is at least two orders of magnitude greater than the previously reported value for the bulk Moon, and the actual source region water contents could be significantly higher.

fluorapatite | lunar water | magma ocean | mare basalt | NWA 773

One of the scientific discoveries resulting from the Apollo missions was the pervasive waterless nature of the Moon and its rocks. The initial studies of the returned samples were pristine and showed no evidence of aqueous alteration, and water analyses were below detection limits. Moreover, hydrous phases were absent from the lunar rocks aside from a few unconfirmed reports of possible amphibole grains (1), which are now considered by many to represent either misidentifications or terrestrial contamination (as summarized by ref. 2). The subsequent forty years of lunar sample analysis have only supported and strengthened the idea that indigenous water was nearly absent from the Moon's interior. In fact, this conclusion has been incorporated into many petrologic and geophysical models constructed to aid in our understanding of lunar formation and lunar geology (3–11). The bulk water content of the Moon was recently estimated to be less than 1 ppb (11), which would make the Moon at least six orders of magnitude drier than the interiors of Earth (12, 13) and Mars (14). This extremely low water content is in keeping with the pervasive volatile-element depletion signature recorded in all lunar materials, because hydrogen is the most volatile of the elements. The exact cause for this volatile-element depletion is still under question; however, many have argued that it stems from the high temperatures associated with the Moon-forming giant-impact event at ~4.5 Ga (i.e., refs. 3, 8, 15, and 16).

Facilitated by advancements in analytical detection sensitivities for water, several recent discoveries have indicated that the story of water on the Moon is far from complete. Evidence for hydroxyl/water on the lunar surface has been detected by using remote sensing data from the Moon Mineralogy Mapper (M^3) instrument on board the Chandrayaan-1 spacecraft (17–19). Moreover, evidence for water within the lunar interior has been reported through ongoing lunar sample analysis efforts. Specifically, up to 46 ppm water has been directly measured in some pyroclastic lunar glasses (16), and hydroxyl has been qualitatively identified

in fluorapatite grains (fluorapatite is a calcium phosphate mineral depicted as [$Ca_5(PO_4)_3F$]) from Apollo 15 mare basalt 15058 (20). Whereas the remote sensing studies are likely providing a glimpse into water formation during space weathering processes, the sample analysis studies provide evidence that the water content of the lunar interior may have been underestimated. Depending on the magnitude of the underestimation, profound changes in our understanding of the Moon's geologic history, from models of lunar formation to our understanding of its thermal and magmatic evolution, may be required.

The current view of lunar formation and its subsequent magmatic evolution begins with the Moon-forming giant-impact event at ~4.5 Ga (i.e., refs. 3, 8, 15, and 16). Following the initial stages of lunar accretion, the lunar-wide magma ocean began to cool and crystallize, marking the start of lunar magmatism and differentiation (21–25). During lunar magma ocean crystallization, it is believed that early-forming ferromagnesian minerals (olivine and pyroxene) sank to the magma ocean floor, resulting in a lunar mantle composed of stratified cumulate mineral layers (21–25). During the middle-to-late stages of magma ocean crystallization, anorthitic feldspar began to crystallize and float to the surface because of its lower density with respect to the residual magma ocean liquid from which it crystallized (21–25). This process resulted in the formation of the lunar ferroan anorthosite lithology that comprises well over 50% of the present-day lunar surface. During the last stages of magma ocean crystallization, the residual liquid became increasingly enriched in incompatible trace elements. These last dregs of unsolidified, incompatible trace element-rich residual liquid are referred to as "urKREEP," which was named after the high abundances of potassium (K), rare earth elements (REE), and phosphorus (P) that were present in the late-stage liquid (as summarized by refs. 10 and 26). In addition to potassium, this residual urKREEP liquid was also enriched in other heat-producing elements such as uranium and thorium, making it an important potential heat source for generating magmatism subsequent to magma ocean crystallization (21–25). Virtually nothing is known about the role of water in the lunar magma ocean. However, given that water is highly insoluble in the major silicates that crystallize from lunar magmas, any water dissolved in the magma ocean liquid should have been concentrated in urKREEP; however, there is currently no quantitative data supporting the presence of water in the urKREEP liquid.

Lunar magmatism continued for at least a billion years (i.e., refs. 10, 27, and 28) after magma ocean crystallization had ceased, resulting in a diverse array of lunar lithologic types (ref. 29 and references therein). It is important to note, however, that all of the lithologies discussed here are within the Procellarum KREEP Terrain (30), a terrain that is not typical of the bulk lunar surface.

GEOLOGY

A number of post magma ocean lithologies even have KREEP-like incompatible trace element signatures, which is typically explained (or partially explained) as resulting from assimilation or mixing of urKREEP with the source magma (21, 22, 31–36). The rock types that are reported to have resulted from this process include KREEP basalts, some Apollo 14 high-aluminum basalts, and the plutonic lithologies of the highlands magnesian suite and alkali suite (21, 22, 31–36). There is also a group of rock types in the Procellarum KREEP Terrain that do not typically exhibit KREEP-like incompatible trace element signatures. These are generally grouped as mare volcanic materials, and they include mare basalts (exclusive of the high-Al basalts) and the pyroclastic fire-fountain glasses (21, 25, 37–39). The two studies that have reported evidence for water in the Moon's interior both investigated igneous materials associated with mare volcanism that do not exhibit KREEP-like incompatible trace element signatures (16, 20). Evidence for elevated water contents in the source regions of the mare materials is profound and supports the possibility of the presence of water in the lunar magma ocean. However, linking mare basalts to the magma ocean is complex, and insight into the water budget of the lunar interior as a whole could be better accomplished by obtaining constraints on the water contents of a variety of lunar rock types, including those with KREEP-like incompatible trace element signatures.

In the present study, apatites from three different lunar samples were analyzed for hydroxyl by using secondary ion mass spectrometry (SIMS). The hydroxyl analyses were subsequently used to infer information about magmatic water contents and the water contents of the magmatic source regions (where possible). The samples investigated here span three distinct rock types, and they all have KREEP-like incompatible trace element signatures. The samples investigated include an Apollo 14 high-Al basalt (14053,16), a clast-bearing impact melt rock (15404,51), and an olivine-gabbro cumulate lunar meteorite (Northwest Africa 2977). The magmatic water contents inferred from this study are compared to previous investigations of water in mare volcanic materials to summarize the current state of knowledge regarding water in the lunar interior.

Results

High-Aluminum Basalt 14053,16. High-Al basalt 14053 is among the most well-studied samples in the lunar collection. Previous petrographic observations have indicated that sample 14053 is a coarse-grained high-Al basalt (40, 41). Previous isotopic studies of the rock have indicated a Rb-Sr crystallization age of 3.92 Ga (e.g., refs. 27 and 42); however, the Sm-Nd isotope systematics were found to be disturbed (43). This observation is anomalous, because normally it is the Rb-Sr system that is prone to disturbance by post-crystallization processes. This dichotomy was considered to reflect the postcrystallization open-system behavior of apatite, which hosts most of the rare earth elements in this rock. The cosmic ray exposure age of 14053 is approximately 21 Ma (44).

Consistent with previous petrographic observations, our analysis confirms this sample to consist primarily of pyroxene and plagioclase with volumetrically minor fayalitic olivine, fluorapatite, baddeleyite, K-feldspar, Fe-Ti oxides, Fe-metal, silica, troilite, and K-Ba-rich glass. Much of the olivine is surrounded by intergrowths of Fe-metal and silica that are likely breakdown products of olivine (Fig. 1A). This texture has been described previously and has been suggested to arise from the rock interacting with solar-wind-implanted hydrogen at the lunar surface during impact-induced shock metamorphism (41).

The apatites in 14053 are typically subhedral to anhedral, and they range in size from ~2 μm to larger than 200 μm in the longest dimension. The fluorapatite is typically associated with late-stage melt pockets that are in the proximity of the olivine, Fe-metal, and silica (Fig. 1). Fluorine, chlorine, and hydroxyl concentrations of the apatites in 14053 were determined by SIMS, and
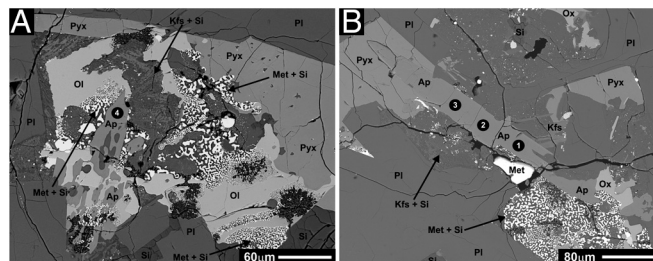

Fig. 1. Back-scattered electron images of Apollo high-Al basalt sample 14053,16. Phase abbreviations are as follows: Ap, apatite; Met, Fe-metal; Met + Si, intergrown Fe-metal and silica; Kfs + Si, intergrown K-rich feldspar and silica; Pyx, pyroxene; Ox, Fe-Ti oxide; Pl, plagioclase; Si, silica; Ol, olivine. (A) BSE image showing one of the apatite grains analyzed by SIMS. The black circle with the white number indicates the analysis spot and its corresponding analysis number. The reduction texture of fayalite breaking down to Fe-metal + silica is also captured in this image. (B) BSE image showing the apatite analyzed by SIMS. The black circles with white numbers indicate analysis spots and their corresponding analysis numbers.

the results are presented in Table 1. The apatites from this sample have fluorine concentrations ranging from 2.48 ± 0.03 to 2.9 ± 0.1 wt%, confirming that these are fluorapatites. The chlorine concentrations of these fluorapatites range from $1,730 \pm 50$ to $4,660 \pm 50$ ppm, and the hydroxyl concentrations range from $1,300 \pm 200$ to $2,700 \pm 400$ ppm. The SIMS analysis spots of apatite from this sample are indicated in Fig. 1.

Alkali-Suite Clast in 15404,51. Apollo sample 15404,51 is a soil grain from the 4–10 mm sieve fraction collected during the Apollo 15 mission; no crystallization or exposure age information is available for this individual grain. This particular grain consists of two lithologies, an impact melt breccia and a lithic clast (Fig. 2A). The lithic clast primarily consists of two pyroxenes and plagioclase that are typically >100 μm in their longest dimension (up to approximately 500 μm). The relative coarse-grained nature of this lithic clast is consistent with it being a plutonic rock. Electron probe microanalysis of the pyroxene and plagioclase were conducted for the purpose of lithologic classification. The pyroxenes in this sample range in Mg number [$Mg_{mol}/(Mg_{mol}+Fe_{mol})$] from 43 to 58, with an average Mg number of approximately 49 (averaged from 15 analyses). The plagioclase compositions ranged from An_{74} to An_{83}, with an average composition of An_{78} (averaged from 12 analyses). On the basis of the plagioclase and pyroxene compositions as well as the coarse-grained nature of the clast (Fig. 2A), this clast is likely a member of the alkali suite from the lunar highlands (Fig. S1, adapted from ref. 45). In addition to the two pyroxenes and the plagioclase, abundant K-rich feldspar and minor silica, fluorapatite, merrillite, Cr-rich spinel, and Fe-Ti oxides are also present in the clast. The texture and mineralogy of this clast are consistent with other alkali-suite samples (i.e., refs. 29, 46, and 47).

Table 1. SIMS analyses of lunar apatite

Sample*	F (wt%)†	Cl (ppm)†	OH (ppm)†
14053_1	2.48 ± 0.03	4,660 ± 50	2,700 ± 400
14053_2	2.70 ± 0.06	4,300 ± 200	1,700 ± 300
14053_3	2.83 ± 0.08	4,570 ± 80	1,400 ± 200
14053_4	2.9 ± 0.1	1,730 ± 50	1,300 ± 200
15404_1	2.47 ± 0.04	11,600 ± 200	1,000 ± 300
15404_2	2.62 ± 0.03	9,340 ± 20	300 ± 200
15404_3	2.54 ± 0.06	10,770 ± 40	220 ± 40
NWA 2977_1	2.7 ± 0.2	2,100 ± 100	7,000 ± 1,000
NWA 2977_2	2.7 ± 0.4	330 ± 50	4,000 ± 700

*Numbers next to the sample refer to the analysis number indicated on the respective BSE image.
†All reported uncertainties are 2σ.

McCubbin et al.

Fig. 2. Back-scattered electron images of Apollo 15 soil grain 15404,51. Phase abbreviations are as follows: Ap, apatite; Pyx, pyroxene; Ox, Fe-Ti oxide; Pl, plagioclase; Mer, merrillite. (*A*) BSE image mosaic showing the two lithologic clast types that occur in sample 15404,51. The alkali-suite clast and impact melt breccia portions of the image are labeled accordingly. (*B*) BSE image showing one of the apatite grains analyzed by SIMS. The black circles with white numbers indicate analysis spots and their corresponding analysis numbers. (*C*) BSE image showing one of the apatite grains analyzed by SIMS. The black circle with the white number indicates the analysis spot and its corresponding analysis number.

Apatite in the alkali-suite clast from 15404,51 exists as anhedral grains, ranging in size from approximately 10 to >100 μm in the longest dimension, and they are typically associated with merrillite (Fig. 2 *B* and *C*). Fluorine, chlorine, and hydroxyl concentrations for the apatites were determined by SIMS, and they are presented in Table 1. The apatites from this sample have fluorine concentrations ranging from 2.54 ± 0.06 to 2.62 ± 0.03 wt%, verifying that these are fluorapatite. The chlorine concentrations of these fluorapatites range from $9,344 \pm 20$ to $10,770 \pm 40$ ppm, and the hydroxyl concentrations range from 220 ± 40 to $1,000 \pm 200$ ppm. The SIMS analysis spots of apatite from this sample are indicated in Fig. 2 *B* and *C*.

Very Low-Titanium Basalt Northwest Africa 2977. Lunar meteorite Northwest Africa (NWA) 2977 is an olivine-gabbro cumulate that is paired with lunar meteorite NWA 773 (48), which contains clasts of the same olivine-gabbro cumulate lithology (49, 50). The crystallization age of the olivine-gabbro cumulate in NWA 773 is 2.86 Ga (51), and no trapped solar wind was detected in this lithology, indicating a very limited residence time at the lunar surface (52). Preliminary reports indicate the same is true for NWA 2977. This rock has bulk chemical characteristics similar to the very low-titanium basalts; however, its incompatible trace element signature is similar to that of KREEP (50, 51), making this a unique sample among other lunar mare basalts (50, 51). The mineralogy of NWA 2977 is broadly consistent with the olivine-gabbro cumulate clasts described in NWA 773, consisting primarily of olivine, pyroxene, and plagioclase. In addition to these phases, merrillite, fluorapatite, baddeleyite, K-feldspar, Fe-Ti oxides, Fe-Ni metal, troilite, and pentlandite are present in minor abundances.

The apatites in NWA 2977 are typically subhedral to anhedral, and they range in size from approximately 5 μm to grains larger than 100 μm in the longest dimension. The apatites typically fill the late-stage mesostasis between the larger olivine, pyroxene, and plagioclase grains, and the apatites commonly coexist with the other minor phases that occur in the meteorite (Fig. 3). Fluor-

Fig. 3. Back-scattered electron images of lunar meteorite sample NWA 2977. Phase abbreviations are as follows: Ap, apatite; Met, Fe-Ni metal; Kfs, K-rich feldspar; Pyx, pyroxene; Ox, Fe-Ti oxide; Pl, plagioclase; Mer, merrillite; Zr, baddeleyite; Ol, olivine. (*A*) BSE image showing one of the apatite grains analyzed by SIMS. The black circle with the white number indicates the analysis spot and its corresponding analysis number. (*B*) BSE image showing one of the apatite grains analyzed by SIMS. The black circle with the white number indicates the analysis spot and its corresponding analysis number.

ine, chlorine, and hydroxyl concentrations for the apatites in NWA 2977 were determined by SIMS, and the results are presented in Table 1. The apatite from this sample have approximately 2.7 ± 0.4 wt% fluorine, verifying that these are fluorapatites. The chlorine concentrations of these fluorapatites range from 330 ± 50 to $2,100 \pm 100$ ppm, and the hydroxyl concentrations range from $4,000 \pm 700$ to $7,000 \pm 1,000$ ppm. The SIMS analysis spots of apatite from this sample are indicated in Fig. 3.

Discussion

Secondary Processes That Could Have Affected Igneous Apatite Compositions. The volatile contents reported in Table 1 demonstrate that none of these lunar samples contain apatite of homogeneous composition, as might be expected from a simple magmatic crystallization history and subsequent behavior as a closed system. Before the analyzed volatile contents of the lunar apatite can be used to infer anything regarding lunar magmas, one must first consider the processes that could have altered the igneous apatite compositions. These processes include both terrestrial contamination that has taken place subsequent to the samples arriving to Earth as well as alteration and/or contamination that could have taken place within the Moon or on the lunar surface. Apatite has been shown to rapidly equilibrate with its geologic surroundings in high-temperature and high-pressure environments (53); however, this equilibration is not likely to occur at ambient terrestrial conditions unless the apatite is nanocrystalline, analogous to that involved in biomineralization processes (54, 55).

Of the three samples studied here, two are Apollo samples and one is a lunar meteorite recovered from a hot desert environment. The Apollo samples were very carefully collected and stored in curatorial facilities with controlled environments for almost the entire duration of their terrestrial history. Therefore, it is extremely unlikely that terrestrial contamination could have altered the apatite compositions within these materials. However, lunar meteorite NWA 2977 has been exposed to a terrestrial weathering environment, and terrestrial contamination and weathering is common for meteorite "finds" (i.e., those not observed to have fallen and immediately collected; see refs. 56 and 57). Although NWA 2977 has not been previously investigated for terrestrial contamination, carbonate deposits have been reported to occur on the exterior portions of lunar meteorite NWA 773 [paired with NWA 2977 (48)], and calcite-rich fracture fillings have also been observed within thin sections of this meteorite (50). Importantly, the silicates in NWA 773 lack observable alteration in thin section, even along fracture boundaries (50), and the same holds true for NWA 2977. Moreover, the Fe-rich Fe-Ni metal grains in both meteorites are intact and unaltered (ref. 50; Fig. 3*B*), which would not be the case if the rocks underwent sufficient contamination to "reset" the volatile contents of the apatite. Therefore, terrestrial

GEOLOGY

contamination has not likely altered or changed the volatile contents of any lunar apatites analyzed in this study.

On the lunar surface, cosmic ray spallation in lunar rocks results in fragmentation of the nuclei of the rock's constituent atoms (predominantly oxygen), and cosmogenic hydrogen is one of the products of this spallation. Given the ≤20 million year exposure ages of 14053 and NWA 2977, we calculate that a maximum of 0.07 ppm H_2O could have been produced in this time (by using the cosmogenic hydrogen production rates of ref. 58). Importantly, this amount of water is far below the water contents of the apatites analyzed in this study.

Postcrystallization alteration of apatite that could have taken place within the Moon or on the lunar surface is potentially more difficult to identify and account for; however, any apatite that shows textural evidence for having reequilibrated with material not indigenous to the apatite-bearing igneous rock will be treated as potentially altered. The most common situation where this might occur is through impact processes; therefore, the effects of shock on apatite should be considered for each sample. All of the samples studied here have experienced some degree of shock or impact processing, and samples with apatites that are in direct contact with an impact melt or showing direct evidence of alteration because of impact processes will be excluded from further consideration in this study. Apatites in the NWA 2977 meteorite do not show evidence for having been affected by post-crystallization reequilibration; however, some of the plagioclase appears to have been transformed to maskelynite, indicating peak shock pressures between 25 and 30 GPa (59). As a comparison, many martian meteorites also have maskelynite, and the apatites within these samples are stoichiometric (i.e., F + Cl + OH = 1), indicating that shock has not played much of a role in changing apatite chemistry in these samples (60–62). Therefore, impact-induced shock will likely have minimal affects on the volatile contents of the lunar apatites in this sample. Sample 15404,51 has an impact melt lithology, although it is not in direct contact with apatite from the alkali-suite clast. In fact, the apatite grains analyzed from 15404,51 are >500 μm from the interface between the two lithologies, and reaction textures between the lithic clast and the impact melt breccia only extend a few microns into the lithic clast. Therefore, direct reequilibration of apatite with the impact melt can be excluded for this sample. Importantly, this does not preclude volatile loss from the apatite as a result of exposure to the high temperatures resulting from the impact event (i.e., hot enough to create an impact melt).

The final sample that we investigated is high-Al basalt 14053. There is some debate as to whether this rock represents the composition of an impact melt (41, 43) or a magmatic liquid (i.e., refs. 32 and 63). However, the sample does display some unique textural features consistent with postcrystallization reequilibration, including a reduction texture involving the breakdown of fayalitic olivine to iron-metal and silica (Fig. 1A). This texture was reported to have resulted from subsolidus hydrogen reduction (41). The energy required for this process is reported to have been supplied by an impact, and the hydrogen source is reported to be solar wind (41). Importantly, it was shown that the phosphates were affected by this process, because they typically have fritted edges, variable REE contents, and disturbed Sm-Nd isotopic systematics where the reduction textures are prominent (41, 43). The observation of the same reduction textures in section 14053,16 (studied here), which are adjacent to the analyzed apatite grains (Fig. 1), indicates that this sample is not appropriate for inferring information about magmatic water contents of a lunar magma, particularly when one of the by-products of the reduction reaction is H_2O. Therefore, the apatite analyses from this sample are not considered further. Sample 15404,51 and NWA 2977 are appropriate for determining the water contents of the magmas from which the apatite crystallized.

Volatile Contents of Lunar Magmas at the Time of Apatite Crystallization. The mineral apatite is structurally depicted as $A[1]_2A[2]_3(BO_4)_3X$ (64), where the X site represents the monovalent anion site typically occupied by fluorine, chlorine, and hydroxyl. Analyses of apatite group minerals can be used to estimate the relative amounts of fluorine, chlorine, and water in coexisting melt, provided apatite-silicate melt partitioning data exist for these volatiles. Several studies have determined the apatite-melt and apatite-fluid partitioning behavior of F, Cl, and OH in terrestrial systems (65–68). Importantly, these studies show that Cl, F, and OH do not partition equally into the apatite X site; thus, the relative volatile abundances of the apatite are not directly proportional to those of the melt. Complicating the issue further, apatite/melt partition coefficients are dependent upon melt composition (i.e., refs. 65 and 67); therefore, understanding the composition of the liquids from which apatite has crystallized is an additional important step in understanding the magmatic volatile load of a given liquid. For basaltic liquids, which represent the closest analogs to the lunar compositions investigated here, $D_F^{apat/basalt}$ = 3.4 and $D_{Cl}^{apat/basalt}$ = 0.8 (67), although the partition coefficient for chlorine is only applicable to basaltic liquids that are fluid-undersaturated. Whereas the $D_{H_2O}^{apat/basalt}$ was not determined in the study in ref. 67, it can be estimated by using the calculated hydroxyl components of the apatite and the minimum melt water contents from each of the experiments; this estimate results in a range of possible apatite-basaltic melt partition coefficients of approximately 0.10–0.25 for H_2O. The larger value is used here because it provides a minimum estimate for the magmatic water contents at the time of apatite crystallization (i.e., we assume $D_{H_2O}^{apat/basalt} \approx 0.25$).

The two samples from the present study deemed appropriate for assessing lunar magmatic water contents had different volatile loads at the time of apatite crystallization. The residual liquid in NWA 2977 contained 7,000–17,000 ppm water, 7,000–9,000 ppm fluorine, and 350–2,800 ppm chlorine at the time of apatite crystallization. In contrast, the residual magma from which the apatite crystallized in the alkali-suite clast in sample 15404,51 contained 200–2,800 ppm water, 7,300–7,800 ppm fluorine, and 11,700–14,800 ppm chlorine. The range in values reported indicates the variability in apatite composition within each sample. Although some of these magmatic volatile contents are quite high, apatite is typically one of the last minerals to enter the phase assemblage of a crystallizing lunar magma. Therefore, the parental magmatic volatile contents of these magmas were significantly lower than the values at the time of apatite crystallization for all three volatiles.

Minimum Water Contents of the Parental Magmas and Lunar Magmatic Source Regions. Water behaves incompatibly during closed-system crystallization of a magma; therefore, parental magmatic water contents can be calculated from apatite if the amount of crystallization that occurred before apatite entered the phase assemblage can be determined (see *SI Text* text for the open-system crystallization scenario). The amount of crystallization before the appearance of apatite is very difficult to determine for the samples analyzed here because one of them is a coarse-grained plutonic rock (alkali-suite clast in 15404,51) and the other is a partial cumulate (NWA 2977), so lower limit estimates on the basis of the modal abundance of apatite will be meaningless. Although we cannot definitively determine when apatite entered the phase assemblage, the parental magmatic water contents can be modeled for each sample as a function of crystallinity (Fig. S2). If, for example, apatite did not enter the phase assemblage until 95% crystallization, the parental magmatic water content for NWA 2977 would range from 360 to 850 ppm H_2O, and the parental magmatic water content for the alkali-suite clast in 15404,51 would range from 10 to 140 ppm H_2O (Fig. S2). These values are similar to the preeruptive magmatic water contents calculated for the

pyroclastic lunar glasses (i.e., 70–745 ppm H_2O depending on the duration of posteruptive degassing 16).

For comparison to the previous estimate of the bulk water content of the Moon (i.e., <1 ppb, from ref. 11), we will take a conservative approach to estimate a minimum parental magmatic water content that assumes 99% crystallization occurred before apatite began to crystallize from the parental magmas of these samples. From this assumption, we can use the range of parental magmatic water contents from Fig. S2 (i.e., 70–170 ppm H_2O for NWA 2977 and 2–28 ppm H_2O for the alkali-suite clast in 15404,51) to calculate the minimum water contents of the magmatic source regions. The water content of the magmatic source region can be calculated as a function of the amount of partial melting that occurred to produce each parental magma composition (Fig. 4). At least a few percent of melting is typically required for partial melts to coalesce and separate from their source (69); therefore, by using 3% as a lower limit of partial melting, we arrive at a minimum range of 60–830 ppb H_2O for the alkali-suite clast source region and a minimum range of 2–5 ppm H_2O for the NWA 2977 source region; assuming closed-system crystallization, apatite is the only H_2O-bearing mineral phase in the assemblage, and apatite began to crystallize from the parent melt after 99% crystallization. For comparison, the pyroclastic glasses analyzed in ref. 16 require a minimum source region water content ranging from 2 to 21 ppm H_2O at 3% partial melting, assuming that the glasses represent partial melt compositions that did not experience any fractionation (Fig. 4). The amount of partial melting could have been much higher than 3% (i.e., ref. 70), which would result in a higher range in water contents for the magmatic source regions (i.e., 10% partial melting would yield a range of 200 ppb to 3 ppm H_2O for the alkali-suite clast source region and a range of 7–17 ppm H_2O for the NWA 2977 source region).

The minimum range in water contents for these lunar magmatic source regions (64 ppb to 21 ppm H_2O) are between two and five orders of magnitude higher than the previous estimate for the bulk water content of the Moon (i.e., <1 ppb, from ref. 11). Moreover, these values are lower limits, and the actual source region water contents could be much higher. The identification of water from multiple types of lunar rocks that display a range of incompatible trace element signatures indicates that

water may be ubiquitous within the lunar interior, potentially as early as the time of lunar formation and magma ocean crystallization.

Materials and Methods

SIMS. The measurements of F, OH, Cl, and C in lunar fluorapatite were performed on a Cameca 6f ion microprobe at the Department of Terrestrial Magnetism, Washington, DC, by using the procedure of ref. 71. The focused (5–10 nA) 10 kV Cs$^+$ primary ion beam was rastered on the sample to a 25 by 25 μm area. The secondary ion beam was extracted at –5 kV from an 8-μm diameter portion of the rastered area with a field aperture. An electron flood gun (–5 kV) was used to compensate for charge buildup in the analysis area. A mass resolution of 6,000 was used to resolve $^{17.003}$[OH] from $^{16.999}$O. Standardization on three terrestrial apatites was performed at the beginning of the session. Information concerning the compositions of the standards used is presented in Table S1, and the calibration curve for hydroxyl (reported as H_2O equivalent) is shown in Fig. S3. The H_2O calibration curve resulted in 2σ uncertainties of about 17%. Each analysis lasted about 10 min. The detection limit for water (~3 ppm H_2O) was determined by analyzing a dry synthetic forsterite crystal (blank) that was mounted with our terrestrial apatite standards; on the lunar thin sections containing apatite, our blank was determined from analyses of coexisting feldspar, pyroxene, or olivine. These analyses gave similar water contents as the synthetic forsterite (<3 ppm). As a result, we estimate our H_2O detection limit at 3 ppm or better for all of the samples analyzed in this study.

Care was taken in the apatite analyses to observe the direct ion image for $^{12.000}$C and $^{34.969}$Cl for every location because grain boundaries and cracks within the sample are clearly illuminated by carbon and chlorine contamination on such surfaces. All of the apatite grains contained cracks; however, it was possible to obtain analyses on reasonably large areas of crack-free apatite within individual grains, and all of the data reported in Table 1 were obtained from such crack-free areas.

Caution should be taken when SIMS analysis is carried out on epoxy mounted thin sections because the possibility exists for OH contamination from the epoxy, which can invade cracks in the sample that may not be visible in the ion probe optics. Therefore, as a precaution, epoxy from each of the lunar thin sections was analyzed in the same way as our standards and unknowns in order to determine C/OH ratios for the epoxy and estimate possible maximum H_2O contributions from epoxy contamination on the surfaces of the thin section. On the basis of these epoxy analyses and the measured C/OH ratios of our apatites, if we assume that all of the C in our apatite analyses comes from epoxy, the maximum contribution is 5% of the total OH, with two exceptions (36% for analysis 14053_4 and 300% for analysis 14503_3). However, the lack of correlation between measured C and OH counts leads us to conclude that epoxy is not the major contributor to our measured C counts; this conclusion is supported by the fact that epoxy used on lunar thin sections is also exceedingly rich in Cl, and there is no relationship between measured carbon and chlorine counts in our apatite analyses. The most likely sources of carbon in our analyses are not epoxy but rather some combination of residual carbon from prior generations of carbon coat and carbon contained in the apatite mineral structure.

A detailed description of the analytical methods employed for classifying the terrestrial apatite standards used for SIMS calibration can be found in SI Text.

Field-Emission Scanning Electron Microscopy. Back-scattered electron (BSE) imaging and energy-dispersive spectroscopy (EDS) were performed at the Geophysical Laboratory, Washington, DC, on a JEOL JSM 6500F scanning electron microscope with a field-emission gun equipped with a liquid N_2-cooled sapphire Si(Li) EDS detector (EDAX). An operating voltage of 15 kV and a beam current of approximately 1 nA was used for all imaging and EDS acquisitions. EDS was used to chemically identify the fluorapatite grains analyzed in this study prior to SIMS analysis.

Fig. 4. Calculated water contents for the magmatic source regions of three lunar magmas, computed as a function of the percentage of partial melting that occurred to generate each of the magmas. For NWA 2977 and the alkali-suite clast in 15404,51, it was assumed that apatite did not begin to crystallize from the parent magmas of these samples until 99% crystallization had occurred. Additionally, it was assumed that the pyroclastic glasses analyzed in ref. 16 are partial melts of their magmatic source region (i.e., did not experience any fractionation). The upper and lower lines for each range represent the range in parental magmatic water contents calculated for each sample. Note that the field for NWA 2977 overlaps a significant portion of the field estimated for the pyroclastic glasses (15).

GEOLOGY

1. Smith JV, Steele IM (1976) Lunar mineralogy: Heavenly detective story part 2. *Am Mineral* 61:1059–1116.
2. Treiman AH (2008) Rhonite in Luna 24 pyroxenes: First find from the Moon, and implications for volatiles in planetary magmas. *Am Mineral* 93:488–491.
3. Albarede F (2009) Volatile accretion history of the terrestrial planets and dynamic implications. *Nature* 461:1227–1233.
4. Taylor SR, Taylor GJ, Taylor LA (2006) The Moon: A Taylor perspective. *Geochim Cosmochim Acta* 70:5904–5918.
5. Bonin B, Bebien J, Masson P (2002) Granite: A planetary point of view. *Gondwana Res* 5:261–273.
6. Elkins-Tanton LT, Chatterjee N, Grove TL (2003) Magmatic processes that produced lunar fire fountains. *Geophys Res Lett* 30:1513.1–1513.4.
7. Kuskov OL (1997) Constitution of the Moon. 4. Composition of the mantle from seismic data. *Phys Earth Planet Int* 102:239–257.
8. Lucey P, et al. (2006) *New Views of the Moon* (Mineralogical Society of America, Chantilly, VA), pp 83–220.
9. Rutherford MJ, Papale P (2009) Origin of basalt fire-fountain eruptions on Earth versus the Moon. *Geology* 37:219–222.
10. Shearer CK, et al. (2006) Thermal and magmatic evolution of the moon. *New Views of the Moon* 60:365–518.
11. Taylor SR, Pieters CM, MacPherson GJ (2006) *New Views of the Moon* (Mineralogical Society of America, Chantilly, VA), pp 657–704.
12. Bolfan-Casanova N (2005) Water in the Earth's mantle. *Mineral Mag* 69:229–257.
13. Williams Q, Hemley RJ (2001) Hydrogen in the deep earth. *Annu Rev Earth Pl Sci* 29:365–418.
14. McCubbin FM, et al. (2010) Hydrous magmatism on Mars: A source of water for the surface and subsurface during the Amazonian. *Earth Planet Sci Lett* 292:132–138.
15. Canup RM (2004) Dynamics of lunar formation. *Annu Rev Astron Astr* 42:441–475.
16. Saal AE, et al. (2008) Volatile content of lunar volcanic glasses and the presence of water in the Moon's interior. *Nature* 454:192–195.
17. Clark RN (2009) Detection of adsorbed water and hydroxyl on the Moon. *Science* 326:562–564.
18. Pieters CM, et al. (2009) Character and spatial distribution of OH/H2O on the surface of the Moon seen by M-3 on Chandrayaan-1. *Science* 326:568–572.
19. Sunshine JM, et al. (2009) Temporal and spatial variability of lunar hydration as observed by the Deep Impact spacecraft. *Science* 326:565–568.
20. McCubbin FM, et al. (2010) Detection of structurally bound hydroxyl in apatite from Apollo mare basalt 15058,128 using TOF-SIMS. *Am Mineral* 95, in press; doi: 10.2138/am.2010.3448.
21. Shearer CK, Papike JJ (1999) Magmatic evolution of the Moon. *Am Mineral* 84:1469–1494.
22. Taylor GJ (2009) Ancient lunar crust: Origin, composition, and implications. *Elements* 5:17–22.
23. Warren PH (1985) The magma ocean concept and lunar evolution. *Annu Rev Earth Pl Sci* 13:201–240.
24. Wood JA, Dickey JS, Marvin UB, Powell BN (1970) Lunar anorthosites. *Science* 167:602–604.
25. Snyder GA, Taylor LA, Neal CR (1992) A chemical-model for generating the sources of mare basalts—Combined equilibrium and fractional crystallization of the lunar magmasphere. *Geochim Cosmochim Acta* 56:3809–3823.
26. Warren PH, Wasson JT (1979) Origin of KREEP. *Rev Geophys* 17:73–88.
27. Nyquist LE, Shih CY (1992) The isotopic record of lunar volcanism. *Geochim Cosmochim Acta* 56:2213–2234.
28. Hiesinger H, Head JW, Wolf U, Jaumann R, Neukum G (2003) Ages and stratigraphy of mare basalts in Oceanus Procellarum, Mare Nubium, Mare Cognitum, and Mare Insularum. *J Geophys Res-Planet* 108:5065.1–5065.27.
29. Papike JJ, Ryder G, Shearer CK (1998) *Planetary Materials* (Mineralogical Society of America, Washington, DC), pp E1–E234.
30. Jolliff BL, Gillis JJ, Haskin LA, Korotev RL, Wieczorek MA (2000) Major lunar crustal terranes: Surface expressions and crust-mantle origins. *J Geophys Res-Planet* 105:4197–4216.
31. Hess PC (1994) Petrogenesis of lunar troctolites. *J Geophys Res-Planet* 99:19083–19093.
32. Neal CR, Kramer GY (2006) The petrogenesis of the Apollo 14 high-Al mare basalts. *Am Mineral* 91:1521–1535.
33. Korotev RL (2005) Lunar geochemistry as told by lunar meteorites. *Chem Erde-Geochem* 65:297–346.
34. Shervais J, McGee JJ (1997) Petrogenesis of alkali-suite anorthosites and norites in the western lunar highlands: Flotation cumulates from pristine KREEP, magma mixing, and assimilation of older anorthosite. *Meteorit Planet Sci* 32:A119–A119.
35. Snyder GA, Neal CR, Taylor LA, Halliday AN (1995) Processes involved in the formation of magnesian-suite plutonic rocks from the highlands of the Earth's moon. *J Geophys Res-Planet* 100:9365–9388.
36. Warren PH (1988) The origin of pristine KREEP: Effects of mixing between urKREEP and the magmas parental to the Mg-rich cumulates. *Proc Lunar Planet Sci* 18:233–241.
37. Delano JW, Livi K (1981) Lunar volcanic glasses and their constraints on mare petrogenesis. *Geochim Cosmochim Acta* 45:2137–2149.
38. Hess PC (2000) On the source regions for mare picrite glasses. *J Geophys Res-Planet* 105:4347–4360.
39. Longhi J (1992) Experimental petrology and petrogenesis of mare volcanics. *Geochim Cosmochim Acta* 56:2235–2251.
40. Bence AE, Papike J (1972) Pyroxenes as recorders of lunar basalt petrogenesis: Chemical trends due to crystal-liquid interaction. *Proceedings of the Third Lunar Science Conference (Supplement 3, Geochim Cosmochim Acta)*, 1 pp:431–469.
41. Taylor LA, Patchen A, Mayne RG, Taylor DH (2004) The most reduced rock from the moon, Apollo 14 basalt 14053: Its unique features and their origin. *Am Mineral* 89:1617–1624.
42. Papanastassiou DA, Wasserburg GJ (1971) RB-SR ages of igneous rocks from Apollo 14 mission and age of Fra Mauro Formation. *Earth Planet Sci Lett* 12:36–48.
43. Snyder GA, Borg LE, Nyquist LE, Taylor LA (2000) *Origin of the Earth and Moon*, eds RM Canup and K Righter (University of Arizona, Tucson), pp 361–395.
44. Eugster O, et al. (1984) Cosmic-ray exposure histories of Apollo 14, Apollo 15, and Apollo 16 rocks. *J Geophys Res* 89:B498–B512.
45. Shearer CK, Papike J (2005) Early crustal building processes on the moon: Models for the petrogenesis of the magnesian suite. *Geochim Cosmochim Acta* 69:3445–3461.
46. Jolliff BL (1991) Fragments of quartz monzodiorite and felsite in Apollo 14 soil particles. *Proc Lunar Planet Sci* 21:101–118.
47. Jolliff BL, Korotev RL, Haskin LA (1991) Geochemistry of 2–4 mm particles from Apollo 14 soil (14161) and implications regarding igneous components and soil-forming processes. *Proc Lunar Planet Sci* 21:193–219.
48. Connolly HC, et al. (2006) The Meteoritical Bulletin, No. 90, 2006 September. *Meteorit Planet Sci* 41:1383–1418.
49. Korotev RL, Zeigler RA, Jolliff BL, Irving AJ, Bunch TE (2009) Compositional and lithological diversity among brecciated lunar meteorites of intermediate iron concentration. *Meteorit Planet Sci* 44:1287–1322.
50. Jolliff BL, Korotev RL, Zeigler RA, Floss C (2003) Northwest Africa 773: Lunar mare breccia with a shallow-formed olivine-cumulate component, inferred very-low-Ti (VLT) heritage, and a KREEP connection. *Geochim Cosmochim Acta* 67:4857–4879.
51. Borg LE, Shearer CK, Asmerom Y, Papike JJ (2004) Prolonged KREEP magmatism on the Moon indicated by the youngest dated lunar igneous rock. *Nature* 432:209–211.
52. Lorenzetti S, Busemann H, Eugster O (2005) Regolith history of lunar meteorites. *Meteorit Planet Sci* 40:315–327.
53. Brenan J (1993) Kinetics of fluorine, chlorine and hydroxyl exchange in fluorapatite. *Chem Geol* 110:195–210.
54. Pasteris JD, et al. (2004) Lack of OH in nanocrystalline apatite as a function of degree of atomic order: Implications for bone and biomaterials. *Biomaterials* 25:229–238.
55. Glimcher MJ (2006) Bone: Nature of the calcium phosphate crystals and cellular, structural, and physical chemical mechanisms in their formation. *Rev Mineral Geochem* 64:223–282.
56. Crozaz G, Floss C, Wadhwa M (2003) Chemical alteration and REE mobilization in meteorites from hot and cold deserts. *Geochim Cosmochim Acta* 67:4727–4741.
57. Rubin AE, Huber H (2005) A weathering index for CK and R chondrites. *Meteorit Planet Sci* 40:1123–1130.
58. Merlivat L, Lelu M, Nief G, Roth E (1976) Spallation deuterium in rock 70215. *Proceedings of the 7th Lunar and Planetary Science Conference* (Pergamon, Oxford), pp 649–658.
59. Milton DJ, Decarli PS (1963) Maskelynite: Formation by explosive shock. *Science* 140:670–671.
60. Boctor NZ, Alexander CMO, Wang J, Hauri E (2003) The sources of water in martian meteorites: Clues from hydrogen isotopes. *Geochim Cosmochim Acta* 67:3971–3989.
61. Leshin LA (2000) Insights into martian water reservoirs from analyses of martian meteorite QUE94201. *Geophys Res Lett* 27:2017–2020.
62. McCubbin FM, Nekvasil H (2008) Maskelynite-hosted apatite in the Chassigny meteorite: Insights into late-stage magmatic volatile evolution in martian magmas. *Am Mineral* 93:676–684.
63. Neal CR, Taylor LA (1992) Petrogenesis of mare basalts: A record of lunar volcanism. *Geochim Cosmochim Acta* 56:2177–2211.
64. White TJ, Dong ZL (2003) Structural derivation and crystal chemistry of apatites. *Acta Crystallogr B* 59:1–16.
65. Webster JD, Tappen CM, Mandeville CW (2009) Partitioning behavior of chlorine and fluorine in the system apatite-melt-fluid. II: Felsic silicate systems at 200 MPa. *Geochim Cosmochim Acta* 73:559–581.
66. Brenan JM (1993) Partitioning of fluorine and chlorine between apatite and aqueous fluids at high-pressure and temperature—Implications for the F and Cl content of high P-T fluids. *Earth Planet Sci Lett* 117:251–263.
67. Mathez EA, Webster JD (2005) Partitioning behavior of chlorine and fluorine in the system apatite-silicate melt-fluid. *Geochim Cosmochim Acta* 69:1275–1286.
68. Zhu C, Sverjensky DA (1991) Partitioning of F-Cl-OH between minerals and hydrothermal fluids. *Geochim Cosmochim Acta* 55:1837–1858.
69. Philpotts AR (1990) *Principles of Igneous and Metamorphic Petrology* (Prentice Hall, Upper Saddle River, NJ).
70. Day JMD, Pearson DG, Taylor LA (2007) Highly siderophile element constraints on accretion and differentiation of the Earth-Moon system. *Science* 315:217–219.
71. Hauri E, et al. (2002) SIMS analysis of volatiles in silicate glasses 1. Calibration, matrix effects and comparisons with FTIR. *Chem Geol* 183:99–114.